





## PAPER

[View Article Online](#)  
[View Journal](#) | [View Issue](#)

# The EFG Rosetta Stone: translating between DFT calculations and solid state NMR experiments†

Javier Valenzuela Reina, <sup>a</sup> Federico Civaia, <sup>a</sup> Angela F. Harper, <sup>a</sup> Christoph Scheurer<sup>a</sup> and Simone S. Köcher <sup>\*ab</sup>

Received 14th April 2024, Accepted 7th May 2024

DOI: 10.1039/d4fd00075g

We present a comprehensive study on the best practices for integrating first principles simulations in experimental quadrupolar solid-state nuclear magnetic resonance (SS-NMR), exploiting the synergies between theory and experiment for achieving the optimal interpretation of both. Most high performance materials (HPMs), such as battery electrodes, exhibit complex SS-NMR spectra due to dynamic effects or amorphous phases. NMR crystallography for such challenging materials requires reliable, accurate, efficient computational methods for calculating NMR observables from first principles for the transfer between theoretical material structure models and the interpretation of their experimental SS-NMR spectra. NMR-active nuclei within HPMs are routinely probed by their chemical shielding anisotropy (CSA). However, several nuclear isotopes of interest, e.g.  $^7\text{Li}$  and  $^{27}\text{Al}$ , have a nuclear quadrupole and experience additional interactions with the surrounding electric field gradient (EFG). The quadrupolar interaction is a valuable source of information about atomistic structure, and in particular, local symmetry, complementing the CSA. As such, there is a range of different methods and codes to choose from for calculating EFGs, from all-electron to plane wave methods. We benchmark the accuracy of different simulation strategies for computing the EFG tensor of quadrupolar nuclei with plane wave density functional theory (DFT) and study the impact of the material structure as well as the details of the simulation strategy. Especially for small nuclei with few electrons, such as  $^7\text{Li}$ , we show that the choice of physical approximations and simulation parameters has a large effect on the transferability of the simulation results. To the best of our knowledge, we present the first comprehensive reference scale and literature survey for  $^7\text{Li}$  quadrupolar couplings. The results allow us to establish practical guidelines for developing the best simulation strategy for correlating DFT to experimental data extracting the maximum benefit and information from both, thereby advancing further research into HPMs.

<sup>a</sup>Fritz-Haber Institute of the Max Planck Society, Berlin, Germany<sup>b</sup>Institut für Energie und Klimaforschung (IEK-9), Forschungszentrum Jülich GmbH, Jülich, Germany. E-mail: s.koecher@fz-juelich.de† Electronic supplementary information (ESI) available. See DOI: <https://doi.org/10.1039/d4fd00075g>

# 1 Introduction

Properties, functionality, and longevity of solid state high performance materials (HPMs) depend critically on their atomistic structure. In order to improve and tailor a material's properties, an understanding of its underlying structure is therefore essential. Solid-state nuclear magnetic resonance (SS-NMR) spectroscopy stands as a pivotal analytical tool in the study of inorganic, organic, and hybrid materials, irrespective of their crystalline or amorphous nature.<sup>5</sup> The technique's inherent sensitivity to local atomic environments, coupled with its non-destructive approach, renders it indispensable for probing the intricate structural details of various materials.<sup>6</sup> Advanced SS-NMR experiments also probe atom dynamics and even allow for *in situ* and *operando* studies.<sup>7</sup>

However, most HPMs, such as battery electrodes or catalysts, exhibit complex, ambiguous SS-NMR spectra due to dynamic effects or amorphous phases. NMR crystallography for such challenging materials requires reliable, accurate, and efficient computational methods for calculating NMR observables from first principles for the transfer between theoretical models of a material and the unambiguous interpretation and analysis of its experimental SS-NMR spectra.<sup>8–10</sup> Furthermore, as the field turns towards predicting NMR spectra using machine learning and surrogate models which take training data from computed NMR quantities, the accuracy of the underlying first-principles computed observables is often considered as a baseline for extrapolation. Therefore, it is critical to provide a reference to the actual experimental values, to avoid compounding errors during the training process.<sup>11</sup>

The local atomistic structure of HPMs is often studied by probing the chemical shielding anisotropy (CSA) of their NMR-active nuclei.<sup>8–10,12–14</sup> The interpretation of the chemical shifts of diamagnetic compounds in SS-NMR experiments with first-principles calculations of the CSA tensors is already well established.<sup>10,12,15,16</sup> However, several nuclear isotopes of interest, *e.g.* <sup>7</sup>Li, and <sup>27</sup>Al, also have a nuclear quadrupole and therefore experience additional interactions with the surrounding electric field gradient (EFG), which are another valuable source of information complementing the CSA.<sup>17</sup> While the isotropic chemical shielding is an indirect probe for the ability of the local electron density to shield the nucleus in an applied magnetic field,<sup>18–20</sup> the quadrupolar coupling is exceptionally sensitive to the symmetry of the electron density distribution and hence a powerful probe for local atomistic environments, structural motifs, and distortions.<sup>21,22</sup> The calculation of quadrupolar coupling also requires less computational effort, since it is based on the ground state electronic structure and does not rely on response theory.<sup>23</sup> But the quadrupolar coupling manifests as complex features in experimental NMR spectra, such as broadened lines or satellite peaks, hence making theoretical simulations indispensable for reliable interpretation and analysis.<sup>2,21,24</sup> There are several examples in the literature which show that experimental quadrupolar parameters in combination with density functional theory (DFT) simulations can be leveraged to perform structure refinement,<sup>25,26</sup> force-field validation<sup>27,28</sup> as well as dynamic<sup>29</sup> and structural investigation<sup>30,31</sup> in complex materials.

In the present work, we study the <sup>7</sup>Li and <sup>27</sup>Al nuclei in detail, since both nuclei play a critical role in high performance energy storage materials, such as solid state electrolytes, state-of-the-art electrodes, and stabilizing coatings.<sup>32–34</sup> We



apply pseudopotential (PP) plane wave DFT codes to calculate the quadrupolar observables in a series of diamagnetic, ionic, Li and Al crystalline compounds and include an extensive literature survey of experimentally determined quadrupolar properties. We chose to limit our study to diamagnetic compounds, as paramagnetic systems require spin-polarized DFT calculations and often yield less accurate experimental results due to fast relaxation and pronounced broadening.<sup>35</sup> The comparison of our simulations with experimental values from literature provides a reference scale and a comprehensive benchmark of the accuracy of the simulation and its dependence on various parameters we tested. Furthermore, we assess the implications of various approximations applied during the computational process.

## 2 Methods

### 2.1 The EFG tensor

For NMR-active nuclei with a nuclear spin  $I > 1/2$ , the nuclear electric quadrupole moment  $Q$  interacts with the local EFG tensor,  $\mathbf{V}$ , which leads to an additional splitting of energy levels in an external magnetic field beyond the Zeeman effect.<sup>36–39</sup> The second-rank, traceless, symmetric EFG tensor describes the gradient of the electric field at the nucleus depending on the surrounding charge distribution as the spatial second derivative of the electrostatic potential  $V(\mathbf{x})$ <sup>40</sup>

$$\mathbf{V} = \frac{\partial^2 V(\mathbf{x})}{\partial x_i \partial x_j}. \quad (1)$$

The eigendecomposition of the EFG tensor  $\mathbf{V}$  provides its eigenvalues and eigenvectors. The latter are a crucial quantity for comparing the calculated tensor with its experimental equivalent, the direction cosines,<sup>41–43</sup> and define the local principal axes system (PAS) of the EFG relative to the crystalline coordinate system. The direction cosines represent the projection of each EFG eigenvector  $\mathbf{V}_i$  on each lattice vector  $\mu_j$  of the studied material.

More commonly studied quadrupolar coupling observables are determined by the three eigenvalues  $V_{ii}$  of the EFG tensor, which are ordered according to<sup>44</sup>

$$|V_{zz}| > |V_{yy}| > |V_{xx}|. \quad (2)$$

The observables are the quadrupolar coupling constant  $C_Q$ , which is defined by the magnitude of the coupling, and the asymmetry  $\eta \in [0,1]$ , which is a measure of the shape of the tensor

$$C_Q = \frac{eQV_{zz}}{h}, \quad (3)$$

**Table 1** Spin  $I$  and nuclear electric quadrupole moment  $Q$  of the  $^7\text{Li}$  and  $^{27}\text{Al}$  isotopes discussed in this paper<sup>45</sup>

Isotope	$I$	$Q/\text{fm}^2$
$^7\text{Li}$	3/2	−4.01
$^{27}\text{Al}$	5/2	14.66



$$\eta = \frac{V_{xx} - V_{yy}}{V_{zz}}, \quad (4)$$

where  $e$  is the elementary charge and  $h$  Planck's constant. Nuclear properties of the studied nuclei  $^7\text{Li}$  and  $^{27}\text{Al}$  are reported in Table 1.

## 2.2 Calculation of EFG tensors

First approaches to correlate experimental NMR observables with specific structural information or motifs started shortly after the invention of NMR spectroscopy. The first correlation and increment schemes were empirical in nature and targeted indirect spin–spin coupling<sup>46,47</sup> and chemical shielding<sup>48–52</sup> mostly restricted to organic molecules. The first *ab initio* calculations of tensorial NMR properties based on the electronic structure near the nucleus relied on local basis sets and were hence technically challenging for the simulation of extended solids.<sup>19,20,53,54</sup>

Crystalline and semi-crystalline (*e.g.* defected, disordered) solid materials are most commonly described in periodic boundary conditions (PBC) utilizing Bloch plane waves<sup>55</sup> to take advantage of the translational symmetry.<sup>56,57</sup> PPs approximate the electron density in the nuclear region by an effective core potential and thereby increase the efficiency of plane wave calculations significantly. However, the concept of PPs approximating the core region is diametrically opposed to simulating NMR observables, which capture interactions of the nuclear spin or quadrupolar moment with the local electron density near the nucleus. Only the introduction of the projected augmented wave (PAW)<sup>58</sup> and the gauge-including projector augmented-wave (GIPAW)<sup>59</sup> methods finally allowed for the simulation of NMR properties of solids in the computationally efficient PP-PBC picture. The PAW formalism reconstructs the electron density in the core region from the optimized pseudo-electron density, while GIPAW adds translational invariance of the magnetic field gauge.<sup>17</sup>

Since NMR parameters are highly sensitive to the electronic structure, any simulation parameter that influences the converged electron density near the nucleus has an impact on the accuracy of the NMR parameter prediction. In particular, small atoms, such as Li, with a small number of electrons, where the distinction between core region and valence electrons becomes vague, are expected to be susceptible to modifications in the electronic structure calculations.

One of the factors which is known to affect the resulting NMR parameter predictions is the atomistic geometry.<sup>60,61</sup> Depending on the material and the method (X-ray diffraction (XRD), neutron scattering), the experimentally determined structure might not be accurate. Hence, first-principles geometry relaxations are sometimes recommended.<sup>9,60</sup>

In this work, we test several simulation parameters and their impact on the accuracy of the resulting quadrupolar coupling. In order to study the effects of geometry, we compare EFG simulations with the unmodified empirical experimental input structures (empir.), optimized structures with fixed experimental lattice vectors and relaxed atomic positions (fixed cell), and fully optimized structures with both relaxed atomic positions and lattice vectors (opt.). While empir. structures determined by XRD usually fail to give reliable positions for light atoms such as hydrogen, a full DFT structure relaxation yields equilibrium



structures at 0 K. Fixed cell structures maintain the room temperature lattice constants adopted from empir. structures, while optimizing atomic positions and in particular equilibrating the coordinates of light atoms.

In addition, we test the influence of exchange–correlation (xc) functionals<sup>4,62–64</sup> (LDA,<sup>65</sup> PBE,<sup>66</sup> PBEsol,<sup>67</sup> PW91,<sup>68</sup> RSCAN<sup>69</sup>), PPs, as well as cell size on the accuracy of the quadrupolar coupling computation and establish a reference scale correlating the results with experimental values from literature.

A similar study was previously conducted for CSA of <sup>7</sup>Li,<sup>15</sup> however for <sup>7</sup>Li quadrupolar  $C_Q$  and  $\eta$  parameters, available literature is significantly sparser. In order to describe the amount of information available for all of the data in our survey, we have classified the <sup>7</sup>Li and <sup>27</sup>Al compounds into two groups according to the extent of information available.

**Group 1:** Crystal structure and experimental values for  $C_Q$  and/or  $\eta$  are available, but not necessarily from the same reference.

**Group 2:** Crystal structure and the full EFG tensor (direction cosines) are available.

As has been previously reported, the accuracy of the nuclear electric quadrupole moment  $Q$  is also critical for comparing experimental and computational  $C_Q$  values.<sup>70,71</sup> But since the  $Q$  values for <sup>27</sup>Al and <sup>7</sup>Li (*c.f.* Table 1) have not changed by more than 1% since 2008,<sup>72,73</sup> we neglect this discussion here.

## 2.3 Computational details

The structures of the Li and Al compounds were extracted from the Materials Project database,<sup>74</sup> the Cambridge Structural Database (CSD)<sup>75</sup> or from the cited references.<sup>21,41–43,76–106</sup>

The EFG calculations and geometry optimizations with CASTEP v23.1<sup>107,108</sup> are converged with respect to the basis set cut-off energy and the Monkhorst Pack  $k$ -point grid. The convergence threshold is set to a variation of less than 5% for  $C_Q$  as well as  $\eta$ . For the geometry optimizations, an energy tolerance of  $2.0 \times 10^{-5}$  eV per atom, a maximum force of  $0.05 \text{ eV } \text{\AA}^{-1}$ , and a stress tolerance of 0.1 GPa per atom are employed. Cut-off energy and  $k$ -point grid are adopted from the EFG calculations. The same procedure is followed for the calculations with Quantum ESPRESSO 7.2<sup>109,110</sup> (QE), using the same convergence criteria. Further computational details are presented in the ESI.†

# 3 Results

## 3.1 <sup>27</sup>Al NMR

<sup>27</sup>Al is one of the best-known and most widely studied quadrupolar nuclei in SS-NMR, both theoretically and experimentally. There is extensive experimental data available in the literature for its quadrupolar observables, both  $C_Q$  and even  $\eta$ .<sup>111</sup> However, to the best of our knowledge, experimental data on its full EFG tensors is rather sparse. Here, we discuss a set of 13 Al compounds of Group 1 and two of Group 2.

Since Al is rather oxophilic, it is preferentially coordinated by oxygen in octahedral  $\text{AlO}_6$  environments, which suggests a small to negligible quadrupolar coupling due to the high local symmetry. But the large nuclear electric



quadrupole moment  $Q$  amplifies even a small  $V_{zz}$ , which might arise from small distortions or a less symmetric crystal space group, to a sizable  $C_Q$ .<sup>112</sup>

Testing the impact of the xc-functional on the calculated  $C_Q$  and  $\eta$  with CASTEP shows that the highly ionic Al compounds studied here are well described by both LDA,<sup>65</sup> GGA (PBE,<sup>66</sup> PBEsol,<sup>67</sup> PW91<sup>68</sup>), and meta-GGA (SCAN<sup>69</sup>) functionals. The standard deviation of  $C_Q$  and  $\eta$  with respect to the applied xc-functional is on the order of 3% and 9%, respectively. The impact of the xc-functional is thus deemed negligible and further calculations are all conducted with PBE.<sup>66</sup>

Similarly, simulations based on the different crystal geometries empir., fixed cell, and opt. derived with CASTEP only yield standard deviations on the order of 6% and 15% for  $C_Q$  and  $\eta$ , respectively. Overall, the fixed cell structures provide the best agreement with experimental reference values. The opt. structures yield the least reliable predictions, since PBE<sup>66</sup> is well known to overestimate interatomic bond lengths<sup>113</sup> and hence allows the cell volume to extend and distort. Lattice parameters of crystalline materials determined experimentally with high confidence are regularly available in literature or databases, discouraging the use of the opt. structures in this case.<sup>114</sup> Since the effect of DFT relaxation, either fixed cell or opt., is minimal, all further calculations are performed with fixed cell structures.

The power of PBC is that they represent an infinitely large defect-free model of a crystalline solid by exploiting the translational symmetry of the Bloch plane waves.<sup>55</sup> Calculations in PBC are usually conducted on the smallest possible unit cell (primitive cell) and expected to yield the same results as a supercell. However, previous studies have shown that cell symmetry and supercell effects can cause numerical errors depending on the implementation of the PBC, grids, and the charge augmentation.<sup>15,115</sup> Hence, the CASTEP EFG calculations are repeated with  $2 \times 2 \times 2$  supercells producing identical results and ruling out any supercell effects in the case of Al.

Al is a third period element with three valence electrons in the 3s and 3p orbitals. The ten electrons of the first and second period orbitals can be considered core orbitals. Correspondingly, the default CASTEP PP (C19) includes those electrons in the effective core potential and only treats the three valence electrons explicitly. The same discrimination is made in the Quantum ESPRESSO PP utilized in this work. Tests using a CASTEP hard PP with eleven electrons being treated explicitly yield a minor decline in agreement with experiment by 0.17 MHz for  $C_Q$ , whereas  $\eta$  remains unaffected. Details can be found in the ESI Table S3.†

In general, the simulations with PBE,<sup>66</sup> fixed cell geometry, and default PP yield a good agreement with experimental <sup>27</sup>Al  $C_Q$  values both for CASTEP and Quantum ESPRESSO calculations as shown in Fig. 1 with a mean absolute error of the linear fit (MAE) of 0.90 MHz (18%) and 1.14 MHz (24%), respectively. Distinct outliers are found for  $\theta$ -Al<sub>2</sub>O<sub>3</sub>,<sup>98</sup>  $\kappa$ -Al<sub>2</sub>O<sub>3</sub>,<sup>78</sup> and AlVO<sub>4</sub><sup>79</sup> (c.f. ESI†), which feature Al on multiple inequivalent crystallographic positions. For  $\kappa$ -Al<sub>2</sub>O<sub>3</sub> and AlVO<sub>4</sub>, comparison of the literature references<sup>78,79,81,116</sup> with the structural data derived from CSD<sup>75</sup> does not allow for an unambiguous assignment of the different crystallographic positions or reveal inconsistencies between different references. Therefore, we neglect  $\kappa$ -Al<sub>2</sub>O<sub>3</sub> and AlVO<sub>4</sub> here.

In comparison to the reference scale for <sup>27</sup>Al  $C_Q$ , the correlation between DFT and experimental values of <sup>27</sup>Al  $\eta$  is considerably less accurate, especially for the



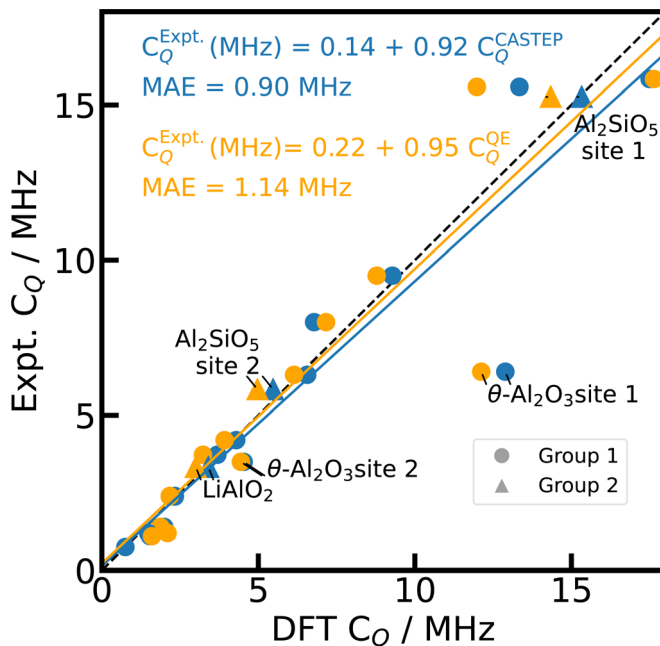


Fig. 1 Reference scale for  $^{27}\text{Al}$   $C_Q$ . The  $^{27}\text{Al}$   $C_Q$  values for 15 Al-containing compounds are simulated with PBE, fixed cell geometries, default PP, and unit cells using CASTEP (blue) and Quantum ESPRESSO (orange). The experimental values from literature can be found in ESI Table S3.†  $\kappa\text{-Al}_2\text{O}_3$  and  $\text{AlVO}_4$  are omitted (see text). The dashed diagonal line indicates the limit of ideal correlation.

mentioned outliers (*c.f.* ESI†), with a MAE of 0.13 and 0.16 (*c.f.* Fig. 2) for CASTEP and Quantum ESPRESSO, respectively. The asymmetry of  $\eta$  is even more sensitive to the local charge distribution and its symmetry than  $C_Q$  as a result of its dependence on all the three components of the EFG tensor (eqn (4)), leading to a more pronounced error propagation of inaccuracies in the electron density. When correlating the individual principal components of the EFG tensor with values derived from experimental  $C_Q$  and  $\eta$  values (ESI Fig. S3†), the larger deviation of  $\eta$  is reflected in the larger errors of  $V_{yy}$ , in particular for the outlier  $\theta\text{-Al}_2\text{O}_3$ .

For  $^{27}\text{Al}$ , we found full experimental EFG tensors for both  $\text{Al}_2\text{SiO}_5$  and  $\gamma\text{-LiAlO}_2$  in the literature<sup>43,117</sup> (Group 2), which provide us with the unique opportunity to not only evaluate the accuracy of the calculated magnitude  $C_Q$  and shape  $\eta$  of the EFG tensor, but also its orientation with respect to the crystal lattice. The experimental references provide the so-called direction cosines of the EFG tensor for each magnetically inequivalent  $^{27}\text{Al}$  site, which can be correlated to the eigenvectors of the EFG tensor. Fig. 3 depicts the comparison of experimental and theoretical direction cosines (red and orange for  $\text{Al}_2\text{SiO}_5$  and pink for  $\gamma\text{-LiAlO}_2$ ). The DFT simulations can reproduce the experimental values with an average error of 5%, and show especially good agreement for  $\gamma\text{-LiAlO}_2$ , which actually outperforms the previous DFT results,<sup>97,118</sup> hence predicting the orientation of the EFG tensor with excellent accuracy.





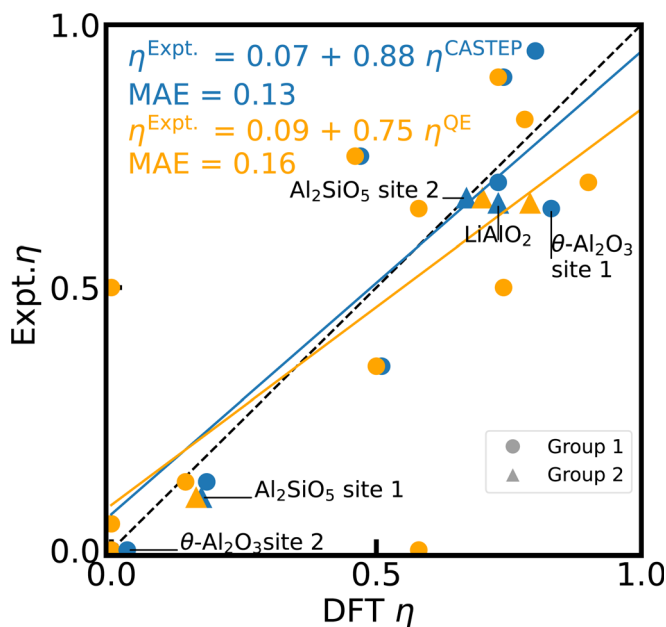


Fig. 2 Reference scale for  $^{27}\text{Al}$   $\eta$ . The  $^{27}\text{Al}$   $\eta$  values for 15 Al-containing compounds are simulated with PBE, fixed cell geometries, default PP, and unit cells using CASTEP (blue) and Quantum ESPRESSO (orange). The experimental values from literature can be found in ESI Table S3.†  $\kappa\text{-Al}_2\text{O}_3$  and  $\text{AlVO}_4$  are omitted (see text). The dashed diagonal line indicates the limit of ideal correlation.

The reliable prediction of quadrupolar observables for  $^{27}\text{Al}$  with good accuracy independent of xc-functional, geometry relaxation, PP, and supercell effect verifies the plane wave, PP method with GIPAW as a robust and useful approach for calculating solid state EFGs. The quantitatively close agreement between CASTEP and Quantum ESPRESSO results proves the reliability of the method independent of the implementation, for  $^{27}\text{Al}$ .

### 3.2 $^7\text{Li}$ NMR

Although  $^7\text{Li}$  and its quadrupolar couplings are not as well studied as  $^{27}\text{Al}$ , quadrupolar  $^7\text{Li}$  SS-NMR plays a crucial role in materials research for Li ion batteries, where Li is the charge carrier.<sup>34</sup> A multitude of different NMR experiments is available that probe the local atomistic structure of  $^7\text{Li}$  as well as its dynamics by addressing either CSA or quadrupolar interactions.<sup>91</sup> *Operando* experiments even allow for tracking charge transport through batteries while cycling.<sup>119</sup>

In contrast to  $^{27}\text{Al}$ , the nuclear electric quadrupole moment  $Q$  for  $^7\text{Li}$  is an order of magnitude smaller, and Li has only three electrons. A small number of electrons presents a challenge when using a Li PP, which divides the electrons into core and valence electrons as well as the electron density in a core and an interstitial region. For the three electrons of Li, this distinction becomes ambiguous. Furthermore, the number of experimental  $^7\text{Li}$   $C_Q$ , and in particular  $\eta$  and explicit EFG tensors components for crystalline, ionic, diamagnetic Li





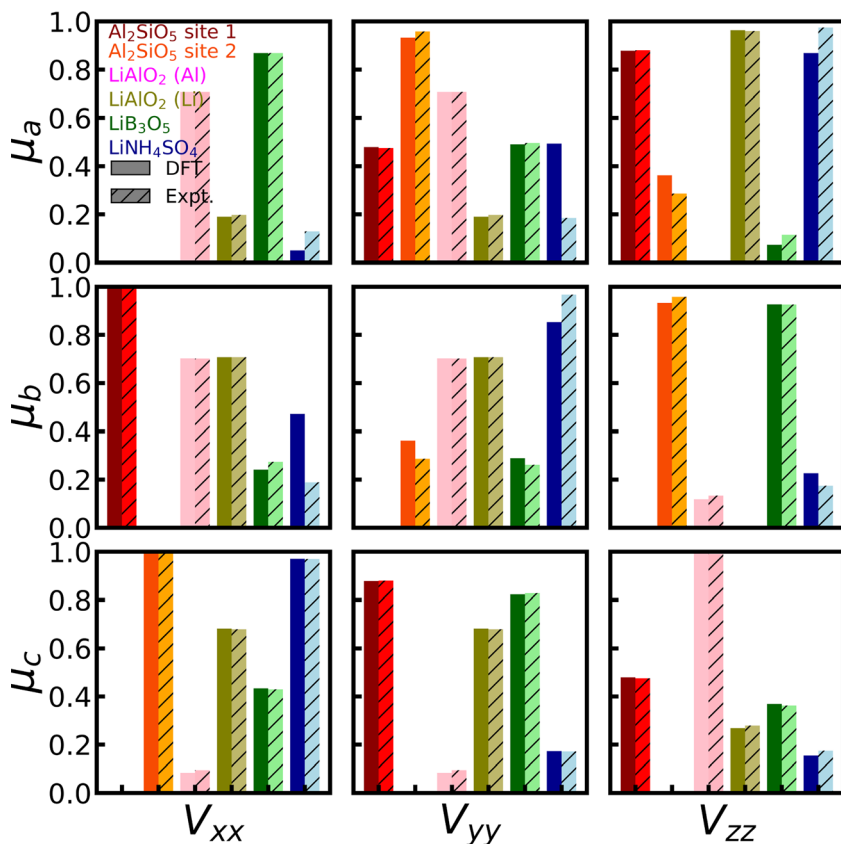


Fig. 3 Orientation of EFG tensors for  $^7\text{Li}$  and  $^{27}\text{Al}$ . The experimentally determined direction cosines of  $\text{LiB}_3\text{O}_5$ ,<sup>41</sup>  $\text{LiNH}_4\text{SO}_4$ ,<sup>42</sup>  $\text{Al}_2\text{SiO}_5$ ,<sup>43</sup> and  $\gamma\text{-LiAlO}_2$ <sup>97</sup> are compared with full EFG tensors calculated with CASTEP, PBE, fixed cell geometry, default PP, and supercells (for  $^7\text{Li}$ ) and unit cells (for  $^{27}\text{Al}$ ). The direction cosines give the projection of each EFG eigenvector  $V_i$  on each lattice vector  $\mu_j$  of the studied material.

compounds available in the literature is limited. In the following, we discuss a set of 23 Li compounds, of which 20 belong to Group 1, and three to Group 2. However, the availability of data for  $\eta$  is extremely sparse.

As already observed for  $^{27}\text{Al}$ , the impact of the xc-functional is negligible for these ionic compounds with standard deviations of 1% and 3% for CASTEP-based  $C_Q$  and  $\eta$ , respectively. PBE<sup>66</sup> is chosen as the default xc-functional for all further analyses (*c.f.* Fig. 4).

Similarly, the details of geometry relaxation are largely irrelevant with a standard deviation of 3% ( $C_Q$ ) and 10% ( $\eta$ ) for empir., fixed cell, and opt. geometries simulated with CASTEP. However, there is one significant exception,  $\text{LiNH}_4\text{SO}_4$ .<sup>42</sup> With the experimental crystal structure adopted from CSD,<sup>75</sup> the calculated  $\eta$  is off by more than factor 3 for the unit cell and gets even worse for the supercell (data not shown). Closer inspection of the crystal structure reveals rather different N–H bond lengths in the  $\text{NH}_4^+$  units, which do not correspond to the structure visualized in ref. 42. Neither the fixed cell nor the opt. structures improve the accuracy



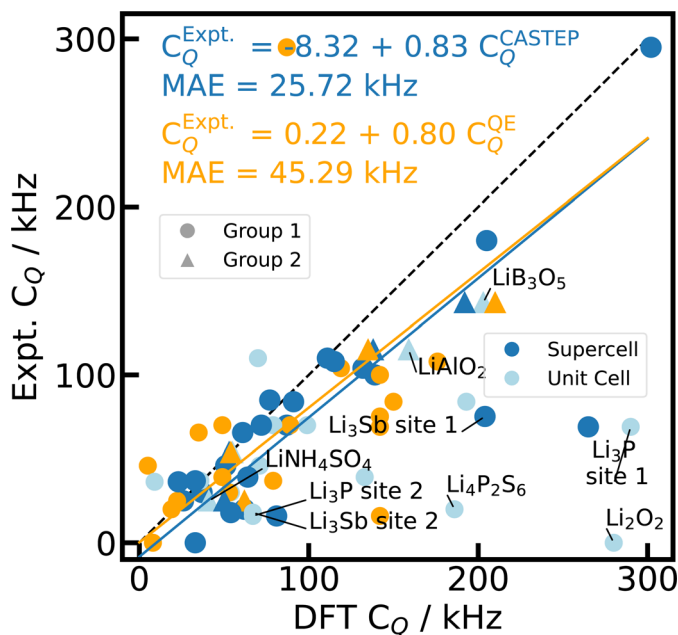


Fig. 4 Reference scale for  ${}^7\text{Li}$   $C_Q$ . The  ${}^7\text{Li}$   $C_Q$  values for 23 Li-containing compounds are calculated with PBE, fixed cell geometries, using CASTEP for unit cells (light blue),  $2 \times 2 \times 2$  supercells (blue), and Quantum ESPRESSO (orange) with the default PP in each case. The experimental values from literature can be found in ESI Table S4.† The dashed diagonal line indicates the limit of ideal correlation. Outliers including  $\text{Li}_3\text{P}$  and  $\text{Li}_3\text{Sb}$  are labelled and described further in the text. The data point for  $\text{Li}_3\text{N}$  [site 1] ( $C_Q = 582$  kHz, ESI Table S4†) is beyond the depicted range, but is included in the regression analysis.

notably with respect to the experimental reference of  $\eta$ . Only a DFT fixed cell relaxation with a relaxed symmetry tolerance allows the N–H bonds to equilibrate, yielding a considerably better agreement with experiment and in particular an improvement by the supercell effect (*c.f.* Fig. 5).

Other striking outliers in the  $C_Q$  correlation (Fig. 4) can be identified as the hexagonal, layered Li pnictide  $\text{Li}_3\text{P}$  and its homologous  $\text{Li}_3\text{Sb}$ <sup>90</sup>. The calculated  $C_Q$  values of the different crystallographic sites are qualitatively correct, matching the Li in the Li–pnictogen layer (P, Sb) with the larger  $C_Q$  value and the Li in the pure Li interlayer with the smaller  $C_Q$  constant. However, the overestimation by DFT simulations amounts to factor 3 to 5. Both  $\text{Li}_3\text{P}$  and  $\text{Li}_3\text{Sb}$  are well-known Li ion conductors, facilitating fast ionic mobility through the pure Li layer, which is known to result in a smaller experimentally observable quadrupolar coupling constant reduced by partial motional averaging.<sup>15,120</sup>  $\text{Li}_3\text{N}$  is also known as a good Li ion conductor, but shows excellent agreement for  $C_Q$  simulated with CASTEP. Here we study the cubic, layered  $\text{Li}_3\text{N}$  phase, rather than one homologous to the hexagonal  $\text{Li}_3\text{P}$  and  $\text{Li}_3\text{Sb}$ , where Li ion mobility up to 300 K takes place predominantly within the Li–pnictogen layer.<sup>121</sup> Including the temperature-dependent influence of ionic mobility on the quadrupolar observables either *via* the vibrational modes,<sup>122</sup> *via* chemical exchange models,<sup>15</sup> or *via* molecular dynamics<sup>12,13,123,124</sup> is beyond the scope of this study.



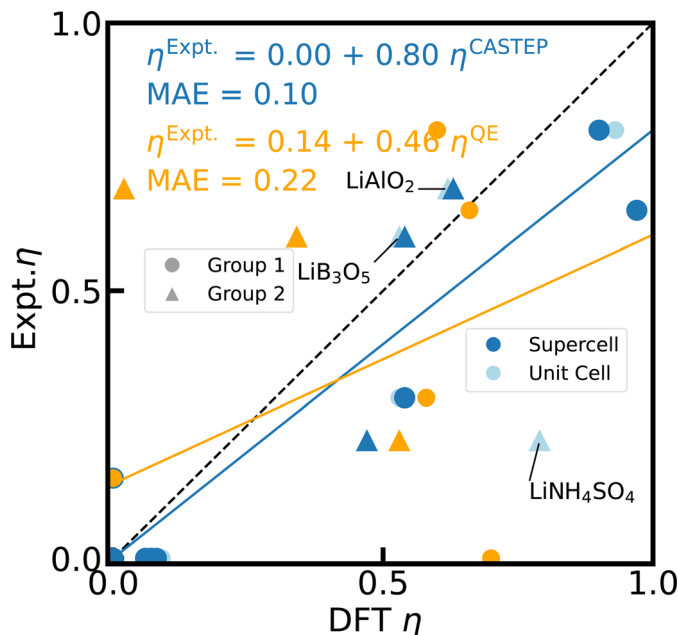


Fig. 5 Reference scale for  ${}^7\text{Li}$   $\eta$ . The  ${}^7\text{Li}$   $\eta$  values for 23 Li-containing compounds are calculated with PBE, fixed cell geometries, using CASTEP for unit cells (light blue),  $2 \times 2 \times 2$  supercells (blue), and Quantum ESPRESSO (orange) with the default PP in each case. For 15 of those compounds, the experimental values from literature can be found in ESI Table S4.<sup>†</sup> The dashed diagonal line indicates the limit of ideal correlation. Outliers including  $\text{LiNH}_4\text{SO}_4$  are labelled and described further in the text.

Even when neglecting the outliers, the correlation of the calculated  $C_Q$  and  $\eta$  with experimental values (Fig. 4 and 5 in light blue) exhibits a major, systematic overestimation of  $C_Q$  and distinct discrepancies of  $\eta$  by up to several orders of magnitude for unit cell simulations. CASTEP calculations with  $2 \times 2 \times 2$  supercells confirm a significant supercell effect, especially for materials with small  $C_Q$  and small unit cells. The supercell effect converges rapidly with cell size as test calculations with  $3 \times 3 \times 3$  supercells corroborate, showing convergence is already achieved for  $2 \times 2 \times 2$ . The effect might result from approximations in the charge augmentation of CASTEP that exceed their physical limit<sup>125</sup> or from long range interactions not correctly captured by the approximations utilized in the PBC implementation. The supercell effect is not observable in Quantum ESPRESSO.

Despite the correction for the supercell effect by using  $2 \times 2 \times 2$  cells, the CASTEP DFT calculations still feature a significant overestimation of  $C_Q$  by about 20% (12% without hex- $\text{Li}_3\text{Pn}$ ) with respect to experimental values. In principle, an inaccurate nuclear electric quadrupole moment  $Q$  for deriving  $C_Q$  from the DFT calculated EFG tensor could explain the discrepancy. However, this overestimation has been observed before<sup>21</sup> for  ${}^7\text{Li}$  as well as other light nuclei, and is usually attributed to a hypothesis formulated in the 1950s by Sternheimer,<sup>126–128</sup> proposing that the polarization of the electronic K-shell induces a secondary quadrupolar moment that shields the nuclear electric quadrupole moment  $Q$ .



This effect cannot be correctly reproduced within the PP approach. Therefore, the PP-GIPAW calculations tend to overestimate  $C_Q$ .

In contrast to  $^{27}\text{Al}$ ,  $^7\text{Li}$  is a second period element with only three electrons in total. The distinction between core and valence electrons becomes ambiguous for such small elements. The default PP of CASTEP (C19) and the one utilized for Quantum ESPRESSO in this work describe all three electrons explicitly as valence electrons. Nevertheless, there is still a core region defined by the core radius which is pseudized. The larger the core radius, the softer the PP and hence the less computationally demanding are the DFT calculations of the electronic structure, since they converge faster with respect to the number of plane waves. On the other hand, a smaller core radius makes the PP harder, potentially improves the description of the electron density in the vicinity of the core, and presumably is better able to capture the polarization near the nucleus. The impact of the core radius was tested for four Li salts by generating a set of modified pseudopotentials with different core radii.<sup>129</sup> The comparison in Fig. 6 shows that reducing the size of the core region can trigger important changes in the predicted EFGs, lowering the calculated  $C_Q$  with only minor impact on  $\eta$  (*c.f.* ESI Fig. S2†). Although these results can be interpreted as a reduction in the overestimation of  $C_Q$ , their reliability requires a more detailed investigation in the Discussion.

For  $^7\text{Li}$ , we could also find experimentally determined eigenvalues of the EFG tensors for  $\text{Li}_2\text{B}_4\text{O}_7$ ,  $\text{LiNbO}_3$ ,  $\text{LiCsB}_6\text{O}_{10}$  (Group 1) and  $\text{LiB}_3\text{O}_5$  (Group 2)<sup>41</sup> (*c.f.* ESI

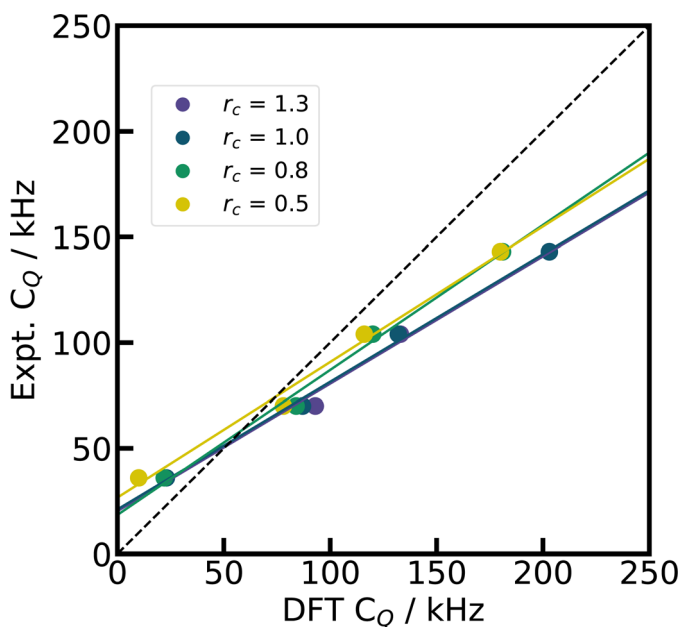


Fig. 6 Test with harder CASTEP PP. By changing the core radius  $r_c$  for the Li PP in CASTEP (default  $r_c = 1.0$ ), we demonstrate the effect of a smaller Li pseudized core region on the simulated  $C_Q$  for four Li compounds ( $\text{LiIO}_3$ ,<sup>96</sup>  $\text{Li}_2\text{CO}_3$ ,<sup>21</sup>  $\text{Li}_2\text{B}_4\text{O}_7$ ,<sup>87</sup>  $\text{LiB}_3\text{O}_5$ <sup>41</sup>), with PBE, fixed cell geometries, and supercells. The dashed diagonal line indicates the limit of ideal correlation.



Table S5†). Together with the principal components  $V_{ii}$  derived from the experimental  $C_Q$  and  $\eta$ , the correlation plot Fig. S4 (ESI)† shows that CASTEP is able to predict these quantities quite reliably. However, the systematic overestimation observed for  $C_Q$  is naturally reproduced by the notable overestimation of  $V_{zz}$ . But also  $V_{xx}$  and  $V_{yy}$  are overestimated, supporting the hypothesis of a shielded nuclear electric quadrupole moment, which does not become apparent in the  $\eta$  correlation in Fig. 5.

For  $\text{LiB}_3\text{O}_5$ ,  $\text{LiNH}_4\text{SO}_4$ , and  $\gamma\text{-LiAlO}_2$ , the full experimental EFG tensors are available in the literature<sup>41,42,97,118</sup> (Group 2). Fig. 3 (blue and greens) shows the comparison of the series of tensors. The DFT simulations can reproduce the experimental values with a MAE of 15% of the experimental values, hence predicting the orientation of the EFG tensor with reasonable accuracy. Nevertheless, also for  $\text{LiB}_3\text{O}_5$ ,  $\text{LiNH}_4\text{SO}_4$ , and  $\gamma\text{-LiAlO}_2$ , we observe the systematic overestimation of the magnitude  $C_Q$  as described before.

In contrast to  $^{27}\text{Al}$ , the quadrupolar coupling of  $^7\text{Li}$  proves to be more challenging to simulate reliably with CASTEP. Geometry relaxation and xc-functional once again do not show any significant impact as such, whereas the case of  $\text{LiNH}_4\text{SO}_4$  demonstrates clearly the crucial importance of the correct representation of local atomistic structure and symmetry in particular on  $\eta$ . However, the CASTEP implementation of PBC does not prove to be robust to supercell effects, providing inaccurate results for primitive unit cell simulations in particular for small  $C_Q$  values. Furthermore, the PP approximation appears to reach its limits for  $^7\text{Li}$ , which presumably results in the systematic overestimation of  $C_Q$  for  $^7\text{Li}$ . Nevertheless, considering the linear correlation between experiment and DFT calculated  $\eta$  values, the choice of approximations and computational schemes implemented in CASTEP performs quite well and predicts  $\eta$  with a MAE of 0.10 and a scaling factor of 0.80.

Quantum ESPRESSO and CASTEP are both PP-GIPAW, plane wave DFT codes, describing the electronic structure within the same basis based on the same physical picture and approximations. Our Quantum ESPRESSO simulations follow the workflow described for CASTEP as closely as possible. The xc-functional and the crystal geometries are identical, while the computational settings and convergence parameters are chosen to reflect the CASTEP ones as accurately as possible. While the results for  $^{27}\text{Al}$   $C_Q$  are almost identical between CASTEP and Quantum ESPRESSO (Fig. 1) and follow a comparable trend for  $^{27}\text{Al}$   $\eta$  (Fig. 2),  $^7\text{Li}$  reveals major discrepancies.

The default GIPAW-PPs of CASTEP and Quantum ESPRESSO for Li and Al are based on the same assignment of core and valence electrons for each element. Nevertheless, other PP key values such as core radius, number and angular momentum of projectors, local and non-local channels as well as the parameterization are not comparable. For  $^{27}\text{Al}$ , transferability between the codes does not suffer despite the different default PPs. The smaller  $^7\text{Li}$  on the other hand is more sensitive to modifications in the PP. Moreover, the sizable supercell effect demonstrated for  $^7\text{Li}$  in CASTEP, which is not detectable in Quantum ESPRESSO, proves that the implementations though based on the same physical descriptions are distinctly different. In order to get comparable accuracy and reliability for  $^7\text{Li}$  EFG calculations in Quantum ESPRESSO, a similar, detailed testing and workflow optimization as described above for CASTEP is necessary but beyond the scope of this work. It is just important to stress that simulation strategies and workflows



cannot necessarily be transferred between codes, even if they are based on the same physical principles.

## 4 Discussion

In recent decades, the PP-GIPAW method has established itself as the standard method for calculating NMR properties for crystalline solid state materials ranging from CSA, indirect spin–spin coupling to quadrupolar coupling.<sup>130–132</sup> At first glance, the PP approximation of the electron density in the core region by an effective core potential appears counterintuitive for simulating interactions of nuclear spin with its environment. However, the reconstruction of the all-electron electron density from the converged, pseudized electron density with the GIPAW method has proven to be an efficient and reliable approach to predict nuclear interactions with robust accuracy for a wide range of materials.<sup>133,134</sup>

Our results for <sup>27</sup>Al  $C_Q$  quadrupolar observables and their excellent agreement with experimental references confirm the PP-GIPAW method as a powerful tool for EFG predictions, supporting NMR crystallography as has been shown before.<sup>135</sup> While <sup>27</sup>Al is one of the most commonly studied quadrupolar nuclei in SS-NMR and well described in the PP picture, our literature survey confirms that <sup>7</sup>Li is not as widely studied and challenges the PP approximation. On the one hand, previous benchmarking has shown accurate predictions of <sup>7</sup>Li chemical shifts with PP-GIPAW methods.<sup>15</sup> On the other hand, the EFG tensor is highly sensitive to small changes and aspherical asymmetries of the electron density near the nucleus,<sup>1</sup> since it depends with  $r^{-3}$  on the charge distribution and its symmetry.<sup>17</sup> Furthermore, it is known that the polarization of the K-shell electrons in a magnetic field induces a local quadrupolar moment, which counteracts the nuclear electric quadrupole moment  $Q$  and yields a reduced effective quadrupole moment.<sup>126–128</sup> The K-shell polarization is most pronounced for first and second period elements. In addition, elements on the left side of the periodic table have been reported to struggle with a precise representation of shallow core states in the plane wave basis, where electrons of the shell below the valence shell ( $n - 1$ ) have semi-core character and need to be described as quasi-valence electrons.<sup>1</sup>

Several examples show that PP-GIPAW predictions of  $C_Q$  for <sup>7</sup>Li and other light nuclei<sup>29,136</sup> suffer from a systematic overestimation.<sup>21</sup> Our simulations exceed the experimental  $C_Q$  by about 20% (12% without hex-Li<sub>3</sub>Pn) on average, which is well in line with reported overestimation factors for <sup>7</sup>Li of 1.20,<sup>21</sup> 1.15,<sup>136</sup> and 1.11.<sup>127</sup>

Specific modifications of the Li PP and CASTEP test calculations with harder PPs support the hypothesis that the systematic overestimation for <sup>7</sup>Li  $C_Q$  might originate from the inadequate description of the K-shell polarization and/or the semi-core states in the default PP picture. However, harder PPs require much larger plane wave basis sets for convergence and hence increase the computational cost by orders of magnitude. Moreover, development of reliable, transferable, robust, and versatile PPs is an art in itself. Our test Li PPs have not been optimized or tested beyond their convergence with cut-off energy and they have not been benchmarked against other properties such as energies, forces, or band structure, not even against other NMR parameters, *e.g.* CSA. The harder Li PPs with smaller core regions have only been used to test the hypothesis that a better, *i.e.* explicit treatment of the electron density close to the nucleus improves the agreement of simulated  $C_Q$  with experimental values. Modifying PPs to improve



agreement with experimental reference values is strongly discouraged, even if it can be physically justified. Instead, linear correlation relationships offer a viable and robust tool to translate between DFT simulated quadrupolar couplings and experimental observables, which is both computationally efficient and transferable to other systems within the limits of the applied methods, settings, and parameters.

The strong sensitivity of the EFG tensor to the local charge distribution is not only expressed in the significance of K-shell polarization and semi-core states, but also in any factor that potentially impacts the accuracy of DFT-derived electronic densities. Several of these factors are computational parameters, which can be converged, such as basis set size, *k*-point grid, integration grid, convergence threshold *etc.*, and are not discussed here. More general computational settings, which cannot be converged, include xc-functional, crystal geometry, and supercell effects. In order to establish a robust and reliable linear interpolation scheme, these factors need to be studied.

For ionic, diamagnetic  $^{27}\text{Al}$  and  $^7\text{Li}$  compounds, we could show that the xc-functional and geometry relaxation have only minor significance and can be disregarded. However, this observation cannot be generalized. Compounds and elements with more covalent type binding character, hydrogen bonds, or  $\pi$ -orbital interactions might not be adequately represented by LDA or GGA but might benefit from hybrid xc-functionals. Naturally, crystal geometry and the local atomic environment has a major impact on the electron density throughout the material as well as close to nuclei. The observed, negligible impact of geometry relaxation arises from the very accurate, experimental crystal structures, where additional first-principles relaxations do not show any major change in atomic coordinates anyway. The most notable exceptions are materials containing hydrogen, such as  $\text{LiNH}_4\text{SO}_4$ , since H does not scatter very well and its position cannot be determined reliably with XRD. Hence, fixed cell optimizations have been reported to improve prediction accuracy of DFT-derived NMR properties.<sup>114</sup>

The supercell effect, which we have introduced above, is a collective term comprising any change in the computed property by simulating supercells or conventional instead of primitive unit cells. Supercell effects might arise from the implementation of integration grids, the treatment of crystal symmetry,<sup>15</sup> charge augmentations,<sup>125</sup> or any physical approximations applied in the PBC, which might be stretched beyond their limits of validity. Besides, supercell effects might only affect certain elements (*e.g.* light elements), certain crystal symmetries (*e.g.* hexagonal) or cells (*e.g.* small unit cells). Therefore, testing for supercell effects is expedient to rule out any obscure inconsistencies between simulation and experiment.

In general, the PP-GIPAW method is verified as a powerful tool for simulating EFG tensors and quadrupolar observables in periodic solids as demonstrated by the good accuracy of the predicted EFG tensor orientations with respect to the crystal lattice. Even for challenging nuclei such as  $^7\text{Li}$ , the PP approach can be successfully applied, if certain measures are taken. With careful benchmarking of the nucleus and material class of interest, a transferable interpolation scheme has to be derived, which is only valid for the specified set of method (*i.e.* software), settings (*i.e.* xc, basis set and *k*-point grid convergence), and approximations (*i.e.* PP, PBC), but can then be utilized for production calculations of unknown, more complex materials.





## 5 Conclusion

The performance and accuracy of the plane wave PP-GIPAW DFT method for computing quadrupolar couplings has been benchmarked before,<sup>31,137</sup> even specifically for <sup>27</sup>Al.<sup>1,116</sup> In this work, we focus on the less well-studied quadrupolar nucleus <sup>7</sup>Li and compare it with the widely known <sup>27</sup>Al, including a comprehensive literature survey and summary of the available experimental data. To the best of our knowledge, we report the first EFG reference scale for <sup>7</sup>Li.

We evaluate the performance of the plane wave PP-GIPAW DFT method, using CASTEP and Quantum ESPRESSO, and investigate not only the magnitude of the quadrupolar coupling  $C_Q$ , but also the shape of the EFG tensor  $\eta$  as well as its orientation given by the experimental direction cosines. Testing the impact of xc-functional, structure relaxation, PP, and supercell effects on the accuracy of the theoretical prediction, the simulations prove to be robust and reliable for <sup>27</sup>Al. <sup>7</sup>Li however exceeds the limits of the PP approximation and shows considerable supercell effects in CASTEP. Based on benchmarking well-known reference substances, we propose practical guidelines for establishing a transferable linear correlation scheme for challenging nuclei such as <sup>7</sup>Li, which can then be applied to translate between theoretical simulations and experimental results of unknown, complex materials. Using this in depth scrutinised and optimized linear correlation scheme, the simulated  $C_Q$  and  $\eta$  for both <sup>7</sup>Li and <sup>27</sup>Al are in good agreement with experiment with an average error on the order of 10% to 20%, while the accuracy of the predicted tensor orientation is excellent.

The PP-GIPAW method competes with all-electron methods, which avoid the PP approximation but are technically more complex for periodic systems and computationally more expensive.<sup>3,17</sup> More recently, solid state cluster embedding methods<sup>138–141</sup> have been developed for NMR properties, which describe the immediate environment of the nucleus of interest at all-electron level and embed it in layered shells of classical molecular mechanics and point charges to mimic the long range interactions of a bulk material. While methodologically rather complex, the embedding method is very promising, especially for aperiodicities such as defects or disorder and for amorphous solid phases.

## Author contributions

Javier Valenzuela Reina: investigation, methodology, writing – original draft, data curation. Federico Civaia: writing – original draft, writing – review and editing. Angela F. Harper: supervision, visualization. Christoph Scheurer: conceptualization, funding acquisition, supervision. Simone S. Köcher: conceptualization, supervision, writing – original draft, writing – review and editing.

## Conflicts of interest

There are no conflicts to declare.

## Acknowledgements

All the authors would like to thank Prof. Chris Pickard, Prof. Jonathan Yates, Dr Philipp Schleker, and Prof. Dr Josef Granwehr for scientific exchange and valuable



discussions. We finally gratefully acknowledge the computational and data resources provided by the Max Planck Computing and Data Facility (MPCDF). AFH would like to acknowledge the support of the Alexander von Humboldt Foundation. JV acknowledges funding by the Bundesministerium für Bildung und Forschung (BMBF) within the Verbundprojekt AdamBatt (FKZ: 03XP0305D). FC and CS would like to acknowledge funding by the Deutsche Forschungsgemeinschaft (DFG, German Research Foundation) within the cluster of excellence EXC 2089: e-conversion.

## References

- 1 P. Blaha, K. Schwarz, F. Tran, R. Laskowski, G. K. H. Madsen and L. D. Marks, *J. Chem. Phys.*, 2020, **152**, 074101.
- 2 M. Profeta, F. Mauri and C. J. Pickard, *J. Am. Chem. Soc.*, 2003, **125**, 541–548.
- 3 P. Blaha, K. Schwarz and P. Herzig, *Phys. Rev. Lett.*, 1985, **54**, 1192–1195.
- 4 A. R. Ferreira, K. Reuter and C. Scheurer, *RSC Adv.*, 2016, **6**, 41015–41024.
- 5 R. Böhmer, K. R. Jeffrey and M. Vogel, *Prog. Nucl. Magn. Reson. Spectrosc.*, 2007, **50**, 87–174.
- 6 B. Reif, S. E. Ashbrook, L. Emsley and M. Hong, *Nat. Rev. Methods Primers*, 2021, **1**, 2.
- 7 L. A. O'Dell and C. I. Ratcliffe, in *NMR of Quadrupolar Nuclei in Solid Materials*, ed. R. E. Wasylshen, S. E. Ashbrook and S. Wimperis, Wiley, Hoboken, NJ, 1st edn, 2012, pp. 213–232.
- 8 S. E. Ashbrook and D. McKay, *Chem. Commun.*, 2016, **52**, 7186–7204.
- 9 R. K. Harris, P. Hodgkinson, C. J. Pickard, J. R. Yates and V. Zorin, *Magn. Reson. Chem.*, 2007, **45**, S174–S186.
- 10 C. Bonhomme, C. Gervais, F. Babonneau, C. Coelho, F. Pourpoint, T. Azaïs, S. E. Ashbrook, J. M. Griffin, J. R. Yates, F. Mauri and C. J. Pickard, *Chem. Rev.*, 2012, **112**, 5733–5779.
- 11 M. C. Venetos, M. Wen and K. A. Persson, *J. Phys. Chem. A*, 2023, **127**, 2388–2398.
- 12 A. F. Harper, S. P. Emge, P. C. Magusin, C. P. Grey and A. J. Morris, *Chem. Sci.*, 2023, **14**, 1155–1167.
- 13 I. Chubak, L. Scalfi, A. Carof and B. Rotenberg, *J. Chem. Theory Comput.*, 2021, **17**, 6006–6017.
- 14 S. A. Southern and D. L. Bryce, *Annu. Rep. NMR Spectrosc.*, 2021, **102**, 1–80.
- 15 S. Köcher, P. Schleker, M. Graf, R.-A. Eichel, K. Reuter, J. Granwehr and C. Scheurer, *J. Magn. Reson.*, 2018, **297**, 33–41.
- 16 C. P. Grey and N. Dupré, *Chem. Rev.*, 2004, **104**, 4493–4512.
- 17 J. W. Zwanziger, in *NMR of Quadrupolar Nuclei in Solid Materials*, ed. R. E. Wasylshen, S. E. Ashbrook and S. Wimperis, Wiley, Hoboken, NJ, 1st edn, 2012, pp. 199–209.
- 18 W. Kutzelnigg, in *Calculation of NMR and EPR Parameters: Theory and Applications*, 2004, pp. 43–82.
- 19 W. Kutzelnigg, *Isr. J. Chem.*, 1980, **19**, 193–200.
- 20 W. Kutzelnigg, U. Fleischer and M. Schindler, in *Deuterium and Shift Calculation*, NMR Basic Principles and Progress, Springer, Berlin, 1990, vol. 23.



- 21 M. T. Dunstan, J. M. Griffin, F. Blanc, M. Leskes and C. P. Grey, *J. Phys. Chem. C*, 2015, **119**, 24255–24264.
- 22 S. E. Ashbrook and S. Sneddon, *J. Am. Chem. Soc.*, 2014, **136**, 15440–15456.
- 23 J. R. Yates and C. J. Pickard, in *eMagRes*, John Wiley & Sons Ltd, 2007.
- 24 M. M. Islam and T. Bredow, *J. Phys. Chem. C*, 2016, **120**, 7061–7066.
- 25 F. A. Perras and D. L. Bryce, *J. Phys. Chem. C*, 2012, **116**, 19472–19482.
- 26 F. A. Perras, I. Korobkov and D. L. Bryce, *CrystEngComm*, 2013, **15**, 8727–8738.
- 27 S. T. Holmes and R. W. Schurko, *J. Phys. Chem. C*, 2018, **122**, 1809–1820.
- 28 S. T. Holmes, C. S. Vojvodin and R. W. Schurko, *J. Phys. Chem. A*, 2020, **124**, 10312–10323.
- 29 J. M. Griffin, A. J. Miller, A. J. Berry, S. Wimperis and S. E. Ashbrook, *Phys. Chem. Chem. Phys.*, 2010, **12**, 2989–2998.
- 30 J. M. Griffin, L. Clark, V. R. Seymour, D. W. Aldous, D. M. Dawson, D. Iuga, R. E. Morris and S. E. Ashbrook, *Chem. Sci.*, 2012, **3**, 2293–2300.
- 31 S. E. Ashbrook, L. L. Pollès, C. J. Pickard, A. J. Berry, S. Wimperis and I. Farnan, *Phys. Chem. Chem. Phys.*, 2007, **9**, 1587–1598.
- 32 S. Stegmaier, R. Schierholz, I. Povstugar, J. Barthel, S. P. Rittmeyer, S. Yu, S. Wengert, S. Rostami, H. Kungl, K. Reuter, *et al.*, *Adv. Energy Mater.*, 2021, **11**, 2100707.
- 33 J. C. Bachman, S. Muy, A. Grimaud, H.-H. Chang, N. Pour, S. F. Lux, O. Paschos, F. Maglia, S. Lupart, P. Lamp, L. Giordano and Y. Shao-Horn, *Chem. Rev.*, 2016, **116**, 140–162.
- 34 F. Blanc, L. Spencer and G. R. Goward, in *NMR of Quadrupolar Nuclei in Solid Materials*, ed. R. E. Wasylshen, S. E. Ashbrook and S. Wimperis, Wiley, Hoboken, NJ, 1st edn, 2012.
- 35 J. Cuny, J. Yates, R. Gautier, E. Furet, E. Le Fur and L. Le Pollès, *Magn. Reson. Chem.*, 2010, **48**, S171–S175.
- 36 P. P. Man, in *Encyclopedia of Nuclear Magnetic Resonance*, ed. D. M. Grant and R. K. Harris, J. Wiley, Chichester, 1996, pp. 3838–3848.
- 37 J. D. Memory, *Quantum Theory of Magnetic Resonance Parameters*, McGraw-Hill, New York, 1968.
- 38 P. Schwerdtfeger, M. Pernpointner and W. Nazarewicz, in *Calculation of NMR and EPR Parameters*, ed. M. Kaupp, M. Bühl and V. G. Malkin, Wiley-VCH, Weinheim, 1st edn, 2004, pp. 279–289.
- 39 K. Schmidt-Rohr and H. W. Spiess, in *Multidimensional Solid State NMR and Polymers*, Acad. Press, London, 1st edn, 1994, pp. 18–21.
- 40 A. Abragam, *The Principles of Nuclear Magnetism*, Oxford University Press, Oxford, 1st edn, 1961.
- 41 A. R. Lim, J. W. Kim and C. S. Yoon, *J. Appl. Phys.*, 2003, **94**, 5095–5099.
- 42 A. Lim, S.-E. Park and S.-Y. Jeong, *Solid State Commun.*, 2000, **113**, 389–394.
- 43 S. S. Hafner, M. Raymond and S. Ghose, *J. Chem. Phys.*, 1970, **52**, 6037–6041.
- 44 R. K. Harris, E. D. Becker, S. M. Cabral de Menezes, P. Granger, R. E. Hoffman and K. W. Zilm, *Pure Appl. Chem.*, 2008, **80**, 59–84.
- 45 M. H. Levitt, *Spin Dynamics*, John Wiley & Sons, 2008.
- 46 M. Karplus, *J. Chem. Phys.*, 1959, **30**, 11–15.
- 47 M. Karplus, *J. Am. Chem. Soc.*, 1963, **85**, 2870–2871.
- 48 D. M. Grant and E. G. Paul, *J. Am. Chem. Soc.*, 1964, **86**, 2984–2990.
- 49 L. P. Lindeman and J. Q. Adama, *Anal. Chem.*, 1971, **43**, 1245–1252.
- 50 W. Bremser, *Anal. Chim. Acta*, 1978, **103**, 355–365.



- 51 A. Ejchart, *Org. Magn. Reson.*, 1980, **13**, 368–371.
- 52 Y. A. Shahab and H. A. Al-Wahab, *J. Chem. Soc., Perkin Trans. 2*, 1988, 255–256.
- 53 M. Schindler and W. Kutzelnigg, *J. Chem. Phys.*, 1982, **76**, 1919–1933.
- 54 M. Schindler and W. Kutzelnigg, *J. Am. Chem. Soc.*, 1983, **105**, 1360–1370.
- 55 F. Bloch, *Z. Phys.*, 1929, **52**, 555–600.
- 56 L. Kleinman and D. M. Bylander, *Phys. Rev. Lett.*, 1982, **48**, 1425–1428.
- 57 D. Vanderbilt, *Phys. Rev. B: Condens. Matter Mater. Phys.*, 1990, **41**, 7892–7895.
- 58 P. E. Blöchl, *Phys. Rev. B: Condens. Matter Mater. Phys.*, 1994, **50**, 17953–17979.
- 59 T. Charpentier, *Solid State Nucl. Magn. Reson.*, 2011, **40**, 1–20.
- 60 F. Vasconcelos, S. Cristol, J.-F. Paul, L. Montagne, F. Mauri and L. Delevoye, *Magn. Reson. Chem.*, 2010, **48**, S142–S150.
- 61 M. Body, C. Legein, J.-Y. Buzaré, G. Silly, P. Blaha, C. Martineau and F. Calvayrac, *J. Phys. Chem. A*, 2007, **111**, 11873–11884.
- 62 F. Tran and P. Blaha, *Phys. Rev. B: Condens. Matter Mater. Phys.*, 2011, **83**, 235118.
- 63 F. Tran, S. Ehsan and P. Blaha, *Phys. Rev. Mater.*, 2018, **2**, 023802.
- 64 R. Laskowski, P. Blaha and F. Tran, *Phys. Rev. B: Condens. Matter Mater. Phys.*, 2013, **87**, 195130.
- 65 W. Kohn and L. J. Sham, *Phys. Rev.*, 1965, **140**, A1133–A1138.
- 66 J. P. Perdew, K. Burke and M. Ernzerhof, *Phys. Rev. Lett.*, 1996, **77**, 3865–3868.
- 67 J. P. Perdew, A. Ruzsinszky, G. I. Csonka, O. A. Vydrov, G. E. Scuseria, L. A. Constantin, X. Zhou and K. Burke, *Phys. Rev. Lett.*, 2008, **100**, 136406.
- 68 J. P. Perdew, J. A. Chevary, S. H. Vosko, K. A. Jackson, M. R. Pederson, D. J. Singh and C. Fiolhais, *Phys. Rev. B: Condens. Matter Mater. Phys.*, 1992, **46**, 6671–6687.
- 69 A. P. Bartók and J. R. Yates, *J. Chem. Phys.*, 2019, **150**, 161101.
- 70 C. Leroy, P. M. Szell and D. L. Bryce, *Magn. Reson. Chem.*, 2019, **57**, 265–267.
- 71 Y. Zhang, S. Mukherjee and E. Oldfield, *J. Am. Chem. Soc.*, 2005, **127**, 2370–2371.
- 72 P. Pykkö, *Mol. Phys.*, 2008, **106**, 1965–1974.
- 73 P. Pykkö, *Mol. Phys.*, 2018, **116**, 1328–1338.
- 74 A. Jain, S. P. Ong, G. Hautier, W. Chen, W. D. Richards, S. Dacek, S. Cholia, D. Gunter, D. Skinner, G. Ceder and K. A. Persson, *APL Mater.*, 2013, **1**, 011002.
- 75 C. R. Groom, I. J. Bruno, M. P. Lightfoot and S. C. Ward, *Acta Crystallogr., Sect. B: Struct. Sci., Cryst. Eng. Mater.*, 2016, **72**, 171–179.
- 76 T. Bräuniger, C. Chandran, U. Wedig and M. Jansen, *Z. Anorg. Allg. Chem.*, 2011, **637**, 530–535.
- 77 D. Müller, E. Jahn, G. Ladwig and U. Haubenreisser, *Chem. Phys. Lett.*, 1984, **109**, 332–336.
- 78 C. V. Chandran, C. E. A. Kirschhock, S. Radhakrishnan, F. Taulelle, J. A. Martens and E. Breynaert, *Chem. Soc. Rev.*, 2019, **48**, 134–156.
- 79 U. G. Nielsen, A. Boisen, M. Brorson, C. J. H. Jacobsen, H. J. Jacobsen and J. Skibsted, *Inorg. Chem.*, 2002, **41**, 6432–6439.
- 80 J. Skibsted, E. Henderson and H. J. Jacobsen, *Inorg. Chem.*, 1993, **32**, 1013–1027.
- 81 B. Ollivier, R. Retoux, P. Lacorre, D. Massiot and G. Férey, *J. Mater. Chem.*, 1997, **7**, 1049–1056.
- 82 R. C. L. Mooney, *Acta Crystallogr.*, 1956, **9**, 728–734.



- 83 Y. Muraoka and K. Kihara, *Phys. Chem. Miner.*, 1997, **24**, 243–253.
- 84 C. Jacoboni, A. Leble and J. Rousseau, *J. Solid State Chem.*, 1981, **36**, 297–304.
- 85 T. M. Gesing and W. Jeitschko, *Z. Naturforsch. B*, 1995, **50**, 196–200.
- 86 A. R. Lim, K. S. Hong, S. H. Choh and S.-Y. Jeong, *Solid State Commun.*, 1997, **103**, 693–698.
- 87 A. R. Lim and I. G. Kim, *Solid State Nucl. Magn. Reson.*, 2015, **66–67**, 40–44.
- 88 M. Leskes, N. E. Drewett, L. J. Hardwick, P. G. Bruce, G. R. Goward and C. P. Grey, *Angew. Chem., Int. Ed.*, 2012, **51**, 8560–8563.
- 89 E. Witt, C. V. Chandran and P. Heitjans, *Solid State Ionics*, 2017, **304**, 60–64.
- 90 G. W. Ossman and A. A. Silvini, *J. Chem. Phys.*, 1971, **54**, 979–982.
- 91 O. E. O. Zeman, I. L. Moudrakovski, C. Hartmann, S. Indris and T. Bräuniger, *Molecules*, 2020, **25**, 469.
- 92 H. Maekawa, S. Kato, K. Kawamura and T. Yokokawa, *Am. Mineral.*, 1997, **82**, 1125–1132.
- 93 H. Eckert, Z. Zhang and J. H. Kennedy, *Chem. Mater.*, 1990, **2**, 273–279.
- 94 T. K. Halstead, *J. Chem. Phys.*, 1970, **53**, 3427–3435.
- 95 A. R. Lim, J. W. Kim and C. S. Yoon, *Solid State Commun.*, 2002, **123**, 505–510.
- 96 T. Minamisono, T. Ohtsubo, Y. Nakayama, S. Fukuda, T. Izumikawa, M. Tanigaki, M. Matsui, S. Takeda, N. Nakamura, M. Fukuda, K. Matsuta and Y. Nojiri, *Hyperfine Interact.*, 1993, **78**, 159–163.
- 97 S. Indris, P. Heitjans, R. Uecker and T. Bredow, *Phys. Rev. B: Condens. Matter Mater. Phys.*, 2006, **74**, 245120.
- 98 L. O'Dell, S. Savin, A. Chadwick and M. Smith, *Solid State Nucl. Magn. Reson.*, 2007, **31**, 169–173.
- 99 D. Müller, W. Gessner, A. Samoson, E. Lippmaa and G. Scheler, *J. Chem. Soc., Dalton Trans.*, 1986, 1277–1281.
- 100 D. Müller, E. Jahn, G. Ladwig and U. Haubenreisser, *Chem. Phys. Lett.*, 1984, **109**, 332–336.
- 101 B. Zhou, B. L. Sherriff, J. S. Hartman and G. Wu, *Am. Mineral.*, 2007, **92**, 34–43.
- 102 J. F. Hon and P. J. Bray, *Phys. Rev.*, 1958, **110**, 624–629.
- 103 G. E. Peterson, P. M. Bridenbaugh and P. Green, *J. Chem. Phys.*, 1967, **46**, 4009–4014.
- 104 M. A. Pimenta, P. Echegut, Y. Luspini, G. Hauret, F. Gervais and P. Abélard, *Phys. Rev. B: Condens. Matter Mater. Phys.*, 1989, **39**, 3361–3368.
- 105 A. R. Lim, S. H. Choh and S. Y. Jeong, *J. Phys.: Condens. Matter*, 1996, **8**, 4597–4602.
- 106 K. Arbi, J. Rojo and J. Sanz, *J. Eur. Ceram. Soc.*, 2007, **27**, 4215–4218.
- 107 S. J. Clark, M. D. Segall, C. J. Pickard, P. J. Hasnip, M. I. J. Probert, K. Refson and M. C. Payne, *Z. Kristallogr. Cryst. Mater.*, 2005, **220**, 567–570.
- 108 S. Sturniolo, T. F. G. Green, R. M. Hanson, M. Zilka, K. Refson, P. Hodgkinson, S. P. Brown and J. R. Yates, *Solid State Nucl. Magn. Reson.*, 2016, **78**, 64–70.
- 109 P. Giannozzi, O. Andreussi, T. Brumme, O. Bunau, M. B. Nardelli, M. Calandra, R. Car, C. Cavazzoni, D. Ceresoli, M. Cococcioni, N. Colonna, I. Carnimeo, A. D. Corso, S. de Gironcoli, P. Delugas, R. A. DiStasio Jr, A. Ferretti, A. Floris, G. Fratesi, G. Fugallo, R. Gebauer, U. Gerstmann, F. Giustino, T. Gorni, J. Jia, M. Kawamura, H.-Y. Ko, A. Kokalj, E. Küçükbenli, M. Lazzeri, M. Marsili, N. Marzari, F. Mauri, N. L. Nguyen, H.-V. Nguyen, A. O. de-la Roza, L. Paulatto, S. Poncé, D. Rocca, R. Sabatini,



- B. Santra, M. Schlipf, A. P. Seitsonen, A. Smogunov, I. Timrov, T. Thonhauser, P. Umari, N. Vast, X. Wu and S. Baroni, *J. Phys.: Condens. Matter*, 2017, **29**, 465901.
- 110 D. Ceresoli, *Daide Ceresoli – Pseudopotentials*, 2024, <https://sites.google.com/site/dceresoli/pseudopotentials>.
- 111 D. Freude and J. Haase, Survey of NMR Parameters for Quadrupolar Nuclei in Powder Materials, in Particular for  $^{27}\text{Al}$ ,  $^{23}\text{Na}$  and  $^{17}\text{O}$ , 2019, <https://dieter-freude.de/quad-nmr/8.pdf>.
- 112 N. Wiberg, A. F. Holleman, E. Wiberg and G. Fischer, *Lehrbuch der Anorganischen Chemie*, De Gruyter, Berlin New York, 102nd edn, 2007.
- 113 P. Haas, F. Tran and P. Blaha, *Phys. Rev. B: Condens. Matter Mater. Phys.*, 2009, **79**, 085104.
- 114 R. K. Harris, E. D. Becker, S. M. C. De Menezes, P. Granger, R. E. Hoffman and K. W. Zilm, *Magn. Reson. Chem.*, 2008, **46**, 582–598.
- 115 W. Ku, T. Berlijn and C.-C. Lee, *Phys. Rev. Lett.*, 2010, **104**, 216401.
- 116 R. Lizárraga, E. Holmström, S. C. Parker and C. Arrouvel, *Phys. Rev. B: Condens. Matter Mater. Phys.*, 2011, **83**, 094201.
- 117 T. Vosegaard, *Prog. Nucl. Magn. Reson. Spectrosc.*, 2021, **123**, 51–72.
- 118 T. Bräuniger, B. Groh, I. L. Moudrakovski and S. Indris, *J. Phys. Chem. A*, 2016, **120**, 7839–7846.
- 119 X. Li, M. Tang, X. Feng, I. Hung, A. Rose, P.-H. Chien, Z. Gan and Y.-Y. Hu, *Chem. Mater.*, 2017, **29**, 8282–8291.
- 120 M. F. Graf, H. Tempel, S. S. Köcher, R. Schierholz, C. Scheurer, H. Kungl, R.-A. Eichel and J. Granwehr, *RSC Adv.*, 2017, **7**, 25276–25284.
- 121 R. Messer, H. Birli and K. Differt, *J. Phys. Colloq.*, 1980, **41**, C6–28–C6–31.
- 122 B. Monserrat, R. J. Needs and C. J. Pickard, *J. Chem. Phys.*, 2014, **141**, 134113.
- 123 A. H. Mazurek, Ł. Szeleszczuk and D. M. Pisklak, *Int. J. Mol. Sci.*, 2021, **22**, 4378.
- 124 C. Lei, A. Erlebach, F. Brivio, L. Grajciar, Z. Tošner, C. J. Heard and P. Nachtigall, *Chem. Sci.*, 2023, **14**, 9101–9113.
- 125 J. Yates, personal communication, 2023.
- 126 R. Sternheimer, *Phys. Rev.*, 1950, **80**, 102–103.
- 127 R. Sternheimer, *Phys. Rev.*, 1951, **84**, 244–253.
- 128 T. P. Das, *Phys. Rev.*, 1956, **102**, 733–738.
- 129 C. Pickard, personal communication, 2023.
- 130 S. E. Ashbrook, L. Le Pollès, R. Gautier, C. J. Pickard and R. I. Walton, *Phys. Chem. Chem. Phys.*, 2006, **8**, 3423–3431.
- 131 S. Sen, *Mol. Simul.*, 2008, **34**, 1115–1120.
- 132 F. Pourpoint, C. Gervais, L. Bonhomme-Courty, F. Mauri, B. Alonso and C. Bonhomme, *C. R. Chim.*, 2007, **11**, 398–406.
- 133 J. D. Hartman, A. Mathews and J. K. Harper, *Front. Chem.*, 2021, **9**, 751711.
- 134 D. V. Dudenko, J. R. Yates, K. D. M. Harris and S. P. Brown, *CrystEngComm*, 2013, **15**, 8797.
- 135 B. Karasulu, S. P. Emge, M. F. Groh, C. P. Grey and A. J. Morris, *J. Am. Chem. Soc.*, 2020, **142**, 3132–3148.
- 136 G. S. Harbison, *J. Magn. Reson.*, 2015, **257**, 24–31.
- 137 K. Choudhary, J. N. Ansari, I. I. Mazin and K. L. Sauer, *Sci. Data*, 2020, **7**, 362.
- 138 A. Dittmer, G. L. Stoychev, D. Maganas, A. A. Auer and F. Neese, *J. Chem. Theory Comput.*, 2020, **16**, 6950–6967.



- 139 M. Kick and H. Oberhofer, *J. Chem. Phys.*, 2019, **151**, 184114.
- 140 D. Berger, H. Oberhofer and K. Reuter, *Phys. Rev. B: Condens. Matter Mater. Phys.*, 2015, **92**, 075308.
- 141 D. Berger, A. J. Logsdail, H. Oberhofer, M. R. Farrow, C. R. A. Catlow, P. Sherwood, A. A. Sokol, V. Blum and K. Reuter, *J. Chem. Phys.*, 2014, **141**, 024105.

